

5-2016

## Development of a phased array using LNBS with non-synchronized clocks

James I. Murray  
*The University of Texas Rio Grande Valley*

Follow this and additional works at: <https://scholarworks.utrgv.edu/etd>



Part of the [Physics Commons](#)

---

### Recommended Citation

Murray, James I., "Development of a phased array using LNBS with non-synchronized clocks" (2016).  
*Theses and Dissertations*. 70.  
<https://scholarworks.utrgv.edu/etd/70>

This Thesis is brought to you for free and open access by ScholarWorks @ UTRGV. It has been accepted for inclusion in Theses and Dissertations by an authorized administrator of ScholarWorks @ UTRGV. For more information, please contact [justin.white@utrgv.edu](mailto:justin.white@utrgv.edu), [william.flores01@utrgv.edu](mailto:william.flores01@utrgv.edu).

DEVELOPMENT OF A PHASED ARRAY USING LNBS WITH  
NON-SYNCHRONIZED CLOCKS

A Thesis

by

JAMES I. MURRAY

Submitted to the Graduate College of  
The University of Texas Rio Grande Valley  
In partial fulfillment of the requirements of the degree of  
MASTER OF SCIENCE

May 2016

Major Subject: Physics



DEVELOPMENT OF A PHASED ARRAY USING LNBS WITH  
NON-SYNCHRONIZED CLOCKS

A Thesis  
by  
JAMES I. MURRAY

COMMITTEE MEMBERS

Dr. Fredrick Jenet  
Chair of Committee

Dr. Volker Quetschke  
Committee Member

Dr. Teviet Creighton  
Committee Member

May 2016



Copyright 2016 James I. Murray  
All Rights Reserved



## ABSTRACT

Murray, James I., Development of a Phased Array Using LNBS with non-Synchronized Clocks. Master of Science (MS), May, 2016, 49 pp., 2 tables, 37 figures, 15 references, 33 titles.

A passive phased array is an array of antennas in which the phases of the signals on each element are controlled to be added to form a spatial beam. The advantage is that one can steer the beam without physically moving the constituent elements as well as create multiple beams on the sky simultaneously. This has application in the field of satellite and spacecraft communications where there is expected to be a large increase in satellite volume due to the increasing access to space. Traditional phased arrays can become costly to synchronize at satellite down-link frequencies, therefore we have built a phased array composed of cheap low noise block-downconverters (LNBS) that uses an external frequency-phase calibration transmitter to synchronize the array. We have shown that the four element array can achieve a factor of sixteen increase in gain over sufficient timescales and can be steered electronically producing the predicted beam.



## TABLE OF CONTENTS

	Page
ABSTRACT.....	iii
TABLE OF CONTENTS.....	iv
LIST OF FIGURES.....	vi
CHAPTER I. INTRODUCTION.....	1
CHAPTER II. DESIGN OVERVIEW.....	4
Receiver Subsystem.....	4
Hardware.....	5
System Temperature and Gain Calculations.....	7
External Clock Transmitter.....	9
Signal Generator.....	11
Frequency Multiplier.....	12
Transmit Horn.....	13
2nd Stage Superheterodyne Receiver.....	14
Bias-T.....	15
Impedance Transformer.....	16
Amplifiers.....	16
Mixers.....	18
Digitizer Subsystem.....	18
Data Analysis.....	19
Beamforming Computation Needs.....	20
Calibration and Beamforming Computational Needs.....	21
CHAPTER III. BEAMFORMING.....	24

CHAPTER IV. CALIBRATION .....	30
Frequency and Phase Calibration.....	31
Coherence Time.....	36
CHAPTER V. DATA .....	38
Array Gain.....	39
Coherence Time.....	41
Beamforming.....	42
CHAPTER VI. CONCLUSIONS .....	44
REFERENCES .....	45
APPENDIX .....	46
BIOGRAPHICAL SKETCH.....	49

## LIST OF FIGURES

	Page
Figure 1: The FuMG 41/42 Mammut Phased Array radar. . . . .	2
Figure 2: A commercially available Low-Noise Block Down Converter. . . . .	5
Figure 3: Tabulated operation modes of a universal LNB. . . . .	6
Figure 4: The linear array of four horns used as the Receiver Sub-system. . . . .	7
Figure 5: Incoherent power measurements . . . . .	10
Figure 6: Spectrum of the received calibration signal. . . . .	11
Figure 7: Block Diagram of the Frequency Multiplier . . . . .	12
Figure 8: The frequency multiplier mounted on the transmit horn . . . . .	13
Figure 9: Frontal view of the transmitting horn . . . . .	14
Figure 10: Schematics for a single channel of the 2nd stage downconverter. . . . .	15
Figure 11: A SPICE Net of the bias-T . . . . .	16
Figure 12: Electrical schematic of a GALI amplifier . . . . .	17
Figure 13: EAGLE software board file showing board layout . . . . .	18
Figure 14: Full four channel superheterodyne receiver. . . . .	19
Figure 15: ROACH board in the configuration described . . . . .	19
Figure 16: Geometry of a uniformly spaced linear array . . . . .	24
Figure 17: Array factor for our array . . . . .	26
Figure 18: Array factor steered toward 7 degrees off zenith . . . . .	27
Figure 19: The element factor modeled by an Airy disk . . . . .	27
Figure 20: Normalized array response at zenith . . . . .	28
Figure 21: Array response at 5 degrees . . . . .	28
Figure 22: Array response at 7 degrees: Steering angle is grating lobe limited . . . . .	29

Figure 23: Calibration Test Set Up . . . . .	30
Figure 24: Results of a frequency calibration . . . . .	31
Figure 25: Error of frequency estimation . . . . .	33
Figure 26: Phase-time plot of an individual horn . . . . .	34
Figure 27: Phase residuals for calibrated data . . . . .	35
Figure 28: Uncalibrated test data . . . . .	36
Figure 29: Calibrated test data . . . . .	36
Figure 30: Phase jumps from dropped data packets . . . . .	38
Figure 31: Raw time series showing the abrupt phase shift . . . . .	39
Figure 32: Time series signal addition . . . . .	40
Figure 33: Plot showing coherent addition of signals . . . . .	40
Figure 34: Gain of the array with and without broadband noise . . . . .	41
Figure 35: Average power of several datasets using the same calibration data . . . . .	42
Figure 36: Power versus steering angle . . . . .	43
Figure 37: Beam null effectiveness . . . . .	43

## CHAPTER I

### INTRODUCTION

The Alliance for Telecommunications Industry Solutions, in American National Standard T1.523-2001, defines the term phased array as A group of antennas in which the relative phases of the respective signals feeding the antennas are varied in such a way that the effective radiation pattern of the array is reinforced in a desired direction and suppressed in undesired directions[1]. There are both fixed beam arrays and electronically scanned arrays. The phases can be varied in analog using components such as phase shifters and electronic line stretchers, or digitally with time or phase shifts. The benefits of a phased array include increased gain and reduced sidelobe levels with the appropriate weighting, fast beam scanning because of the lack of mechanical steering involved, the ability to form multiple beams simultaneously, and durability: if a single component fails, the array as a whole still functions, although with reduced gain and beam resolution.

The concept phased array transmission was first introduced in 1905 by Nobel laureate Karl Ferdinand Braun who was able to demonstrate the enhanced transmission of radio waves in a specific direction. In his 1909 Nobel Lecture he described how he arranged three antennas in such a way as to create a directional signal[2]. This was the first fixed-beam phased array. Others such as Marconi had been experimenting with fixed-beam arrays since 1906[13]. In his paper titled "Directive Antenna" Marconi explored array technology as a means of improving long range telecommunications through improved directivity. Although it can be said that the modern champion of the development of phased array technology is radar development, early advancements of phased array technology were developed in the context of short-wave radio telecommunications, such as Friis' 1925 paper "A New Directional Receiving System"[14] where

he described a two-element array composed of 1.76 meter diameter loop antennas placed 34.4 meters apart, operating at a 492 meter wavelength. This array was not steered electronically, but mechanically. In the 1930's electronic steering was explored in papers such as "Experiments with directivity steering for fading reduction" by Bruce and Beck in 1935[15] and "A Multiple Unit Steerable Antenna for Short-Wave Reception" by Friis and Feldman in 1937[12]. Phased array research really took off during World War II, where the benefits applied to radar implementations were explored. The FuMG 41/42 Mammut was the first long-range phased-array early warning radar, built by Germany around 1944 near the end of World War II[3].

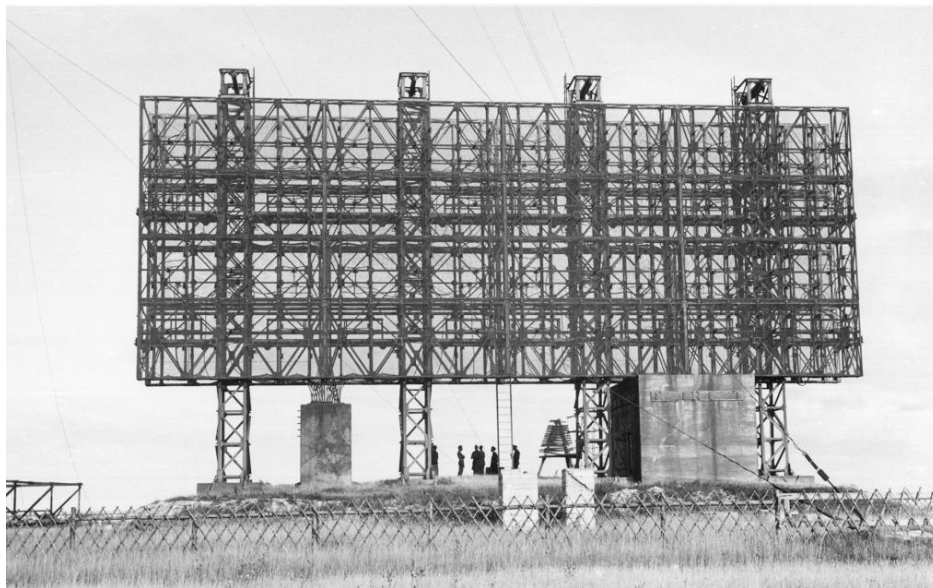


Figure 1: The FuMG 41/42 Mammut Phased Array radar.

Currently, phased-array antennas are being used in AM and FM radio broadcasting to increase gain and give broadcast beams a slightly downward tilt. So called smart antennas that use adaptive beamforming techniques and active null placement are being used for cellular telephone networks. The United States Navy employs the AN/SPY-1 on its destroyers which "is able to perform search, track and missile guidance functions simultaneously with a capability of over 100 targets." [4] With current surge in interest in space exploration and the elevated number of satellites being launched into orbit, the phased array can find application in the field of

spacecraft tracking and satellite communications.

The usefulness of communications satellites directly scales with our ability to download data from them. A phased array can rapidly track a satellite and increase the number of independent links made simultaneously, which increases the total communication bandwidth through spatial filtering. One of the drawbacks of implementing a phased array system is the cost associated with implementing a receiver chain for each array element. As frequency increases the cost of individual components also increases. Additionally, the clocks and oscillators in each of the receiver chains need to be synchronized, which becomes more difficult as frequency increases. Commercial low-noise block downconverters (LNBS) are incredibly cheap and are used for single-antenna satellite communications. An array of LNBS could be a cheap alternative to developing an entire Ku band receiver. The caveat is that each LNB has an independent oscillator performing the initial down conversion. To correct for this we have developed a calibration technique that allows us to digitally synchronize the frequencies and phases of the signals by using an external transmitter to act as a phase and frequency reference for the individual elements. Once a calibration dataset has been taken and analyzed, the resulting corrections can be implemented simultaneously with the beamforming phase offsets, without a significant increase in the number of flops (floating-point operations per second) needed to calibrate and beamform in real time. The main features of this system include the use of cheap off-the-shelf LNBS and calibration using an external transmitting source. It has also been designed in such a way as to be easily expandable to detect multiple targets and simultaneous track and download from multiple sources. The remainder of this document will expound on the hardware design and testing, calibration algorithms, beamforming techniques, and preliminary results.

## CHAPTER II

### DESIGN OVERVIEW

The design of the phased array antenna can be broken down into several subsystems. The subsystems, which are described in greater detail below, are the

- Receiver Subsystem: Used for initial reception of a Ku band signal
- External Clock Transmitter: Used to calibrate the LNB clock offsets
- 2nd Stage Superheterodyne Receiver: Brings signals down to baseband
- Digitizer Subsystem: Digitizes and ships the signal to a CPU
- Data Analysis: Calibrates, steers the beams, and saves the data

Theoretical calculations indicate that the array will have a peak gain of 28.49 dBi and a system noise temperature of about 50.9 K. This leads to a prediction for the minimum detectable equivalent isotropically radiated power (EIRP) of 44.43 dBW. Since a typical free-to-air geostationary satellite has total EIRP power outputs of 0.003 W/Hz, we can refer to the Appendix and see that there are many detectable satellites from our location.

#### **Receiver Subsystem**

In the following section we will describe the hardware of the receiver subsystem. Then we will derive the expected system gain and temperature. From this we will be able to estimate the minimum detectable EIRP for our array.

## Hardware

The receiver subsystem is composed of a 4-element linear array of commercial LNBS similar to the one shown in Fig. 2.



Figure 2: A commercially available Low-Noise Block Down Converter.

Although each LNB has its own free running clock, there are still several advantages to using this commercially-available piece of hardware. It is cheap, usually around \$15 per LNB, which receives from 10.7–12.75 GHz, dual polarization, has 70 dB gain and heterodynes to a more manageable 950–2150 MHz. Compare this to something like the Minicircuits ZX05-153+ at \$50, which is just a satellite downlink mixer, or the ZX60-14012L-S+ amplifier at \$180, which only has about 12 dB of gain. The frequency band (high band or low band) and the

polarization can be chosen by the bias voltage and the inclusion of a 22 kHz tone into the LNB, which is detailed in the following table.

Supply		Block		Local oscillator frequency	Intermediate freq. range
Voltage	Tone	Polarization	Frequency band		
13 V	0 kHz	Vertical	10.70–11.70 GHz, low	9.75 GHz	950–1,950 MHz
18 V	0 kHz	Horizontal	10.70–11.70 GHz, low	9.75 GHz	950–1,950 MHz
13 V	22 kHz	Vertical	11.70–12.75 GHz, high	10.60 GHz	1,100–2,150 MHz
18 V	22 kHz	Horizontal	11.70–12.75 GHz, high	10.60 GHz	1,100–2,150 MHz

Figure 3: Tabulated operation modes of a universal LNB.

In addition to the phenomenal gain and reception bandwidth of the LNBs, they also have a noise figure of 0.2 dB, which is low enough that it will have minimal effect on the signal-to-noise ratio of our signal, and when combined with the LNBs high gain, will dominate the overall noise figure of the system. The array is a linear array with each horn being spaced 10 cm from each other as shown in Fig. 4. They are mounted on a powder-coated aluminum rack-mountable plate to secure the array to the equipment rack for testing.

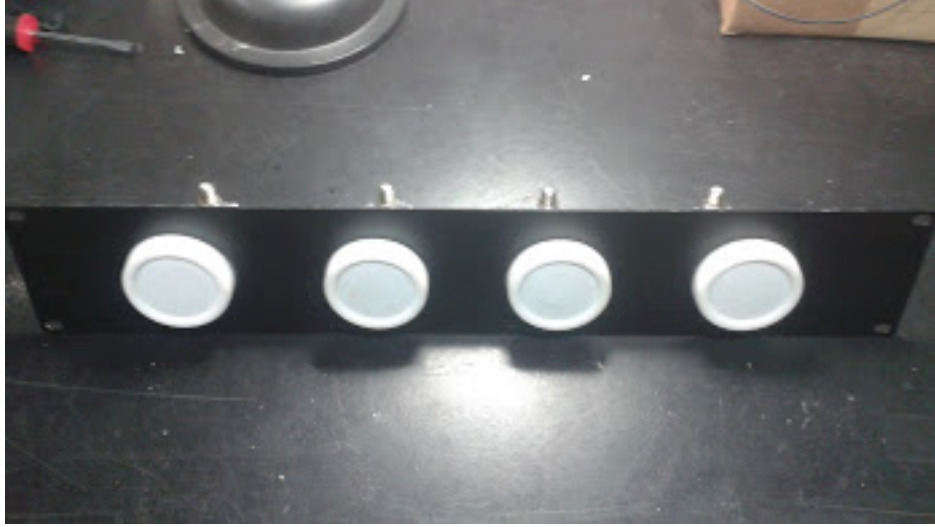


Figure 4: The linear array of four horns used as the Receiver Sub-system.

### System Temperature and Gain Calculations

To calculate the theoretical system gain and temperature we can start by approximating the power pattern of an individual horn with the normalized intensity pattern of an Airy disk as shown in Eq. 1, where  $J_1(x)$  is the Bessel function of the first kind,  $k$  is the wave number,  $a$  is the aperture radius, and  $\theta$  is the angle measured from the peak of the disk.

$$G = \left( \frac{2J_1(ka \sin(\theta))}{\sin(\theta)} \right)^2 \quad (1)$$

Since we are interested in the peak directivity, we will evaluate  $G$  in the limit as  $\theta \rightarrow 0$ , which yields

$$\begin{aligned}
G_{\text{peak}} &= \lim_{\theta \rightarrow 0} G \\
&= \lim_{\theta \rightarrow 0} \left( \frac{2J_1(ka \sin(\theta))}{\sin(\theta)} \right)^2 \\
&= \lim_{\theta \rightarrow 0} (ka(J_0(ka \sin(\theta)) - J_2(ka \sin(\theta))))^2 \\
&= (ka)^2 \\
&= 44.15 = 16.45\text{dBi}
\end{aligned} \tag{2}$$

for a frequency of 10 GHz and  $a = 3.175\text{cm}$ . If we assume the noise figure of the LNB is 0.2 dB, as given by the manufacturer, we can calculate the system temperature as

$$\begin{aligned}
T_{\text{sys}} &= 270(10^{NF} - 1) \\
&= 12.72\text{K}
\end{aligned} \tag{3}$$

where NF is the noise figure. The effective collecting area,  $A_e$ , of an antenna is given by

$$\begin{aligned}
A_e &= G \frac{\lambda^2}{4\pi} \\
&= \pi a^2
\end{aligned} \tag{4}$$

when we plug in Eq. 2. The received Signal-to-Noise Ratio,  $SNR$ , of the antenna is related to the effective area by

$$SNR = \frac{A_e F}{k_b T} \tag{5}$$

where  $F$  is the flux per unit area per unit hertz,  $k_b$  is the Boltzmann constant, and  $T$  is the temperature. If we plug Eq. 4 into Eq. 5 and note that for  $N$  identical antennas,  $G$  increases as  $N^2$  while  $T$  only increases as  $N$ , we see that the  $SNR$  increases as  $N$ . Therefore, for our  $N = 4$  element array the gain should increase to 28.49 dBi and the system temperature to 50.9 K. Now we can derive a minimum detectable Equivalent Isotropic Radiated Power,  $EIRP$ , by defining it as the  $EIRP$  that would yield an  $SNR$  of 1. The resulting flux  $F$  is

$$F = \frac{1}{4\pi r^2} \frac{EIRP}{BW} \quad (6)$$

where  $r$  is the distance to the transmitter and  $BW$  is the bandwidth of the receiver. After rearranging Eq. 6 and substituting Eq. 5 we get for the minimum detectable  $EIRP$

$$\begin{aligned} EIRP_{\min} &= 4\pi r^2 \frac{k_b T BW}{NA_e} \\ &= 44.3 \text{dBW} \end{aligned} \quad (7)$$

where  $r = 3.6 \times 10^7$  m and  $BW = 30$  MHz.

### External Clock Transmitter

Each of the free running clocks in the LNBS not only has a relative phase difference, but also has a slight frequency offset. If this is not corrected, it will impede our ability to properly beamform. In order to achieve the gains that come from coherent addition of signals, the signals must be sufficiently correlated. If we consider two signals  $a(\omega)$  and  $b(\omega + \Delta\omega)e^{i\omega\Delta t}$  of equal amplitude, where  $a$  and  $b$  are correlated, and look at the power of the sum of the two signals we have

$$|a(\omega) + b(\omega)e^{i\omega\Delta t + \Delta\omega t}|^2 = |a|^2 + |b|^2 + (a^*b)e^{i(\omega\Delta t + \Delta\omega t)} + (b^*a)e^{-i(\omega\Delta t + \Delta\omega t)} \quad (8)$$

When taking an average over many cycles, the first two terms are unchanged. For the second two terms however, 3 scenarios exist. First, if  $\Delta\omega$  and  $\Delta t$  are non-zero, the  $\Delta\omega$  term causes them to average to zero leaving a gain of  $N = 2$  and no increase in  $SNR$ . Second, if  $\Delta\omega$  is zero but  $\Delta t$  is not, the result is a gain of  $2(1 + \xi)$  where  $\xi$  is the correlation coefficient between  $a$  and  $b$  (which depends on  $\Delta t$  but is constant in time). Third, if  $\Delta\omega$  and  $\Delta t$  are zero, the result is an  $N^2 = 4$  gain in the power. From these illustrations we see the effects of phase-frequency incoherence on signal addition.

To verify that the horns could not be used without calibration we performed a test where we compared the signals of a signal LNB to that of four LNBs added with an analog signal combiner. First we looked at a signal that would not be correlated among the LNBs; specifically, self-noise. Then we used a fluorescent light bulb as a broadband noise generator to inject a correlated signal into the LNBs. The fluorescent bulbs make excellent microwave noise sources as shown in the MIT VSRT memo series[6] and can have noise temperature in excess of 10,000 K[5]. The results are shown in Fig. 5, where we see about 6 dB increase in signal strength for the uncorrelated signals, which is expected for four array elements. The correlated signal, however, also only shows a 6 dB increase, which indicates that uncalibrated horns turn correlated inputs into uncorrelated outputs.

### Coherence Test

	Light Off (dBm)	Light On (dBm)
<b>LNB Single</b>	-36.13	-35.51
<b>LNB Array</b>	-30.25	-29.88
<b>Difference</b>	5.88	5.63

Figure 5: Incoherent power measurements

In traditional phased array receivers, frequency coherence is achieved by feeding the mixers in the individual receiver chains with the same oscillator, or having each oscillator locked to a reference through some sort of feedback loop. Phase coherence is maintained by making each receiver chain as close to the same electrical length as possible, as well as using filters that minimize delays that result in non-linear phase-frequency relationships. Since our LNBs have independent clocks, we have crafted a transmitter to act as a phase-frequency reference for the array. Each antenna can lock on to the calibration signal and determine its offsets by declaring one horn to arbitrarily have the "correct" frequency and phase, and aligning the others to this arbitrary reference. This works because no absolute phase-frequency information is necessary to

achieve coherence between antennas. Only relative phase-frequency information is needed. The external clock transmitter consists of a relatively low-frequency signal generator, a frequency multiplier to bring the L band tone up to a Ku band tone, and a transmitting horn.

## Signal Generator

We used an FSH-3 Spectrum Analyzer with Tracking Generator set in the Tracking Generator test mode and the sweep span equal to 0. This effectively makes the FSH-3 acts as a continuous wave (CW) tone generator, with the exception that the waveform is not as pure as a dedicated CW generator, as can be seen in Fig. 6. The signal generator would ideally be a dedicated CW tone RF signal generator, but due to limited resources, the FSH-3 was able to be used as a sub-optimal replacement. The fundamental frequency was set to 1960833333 Hz.

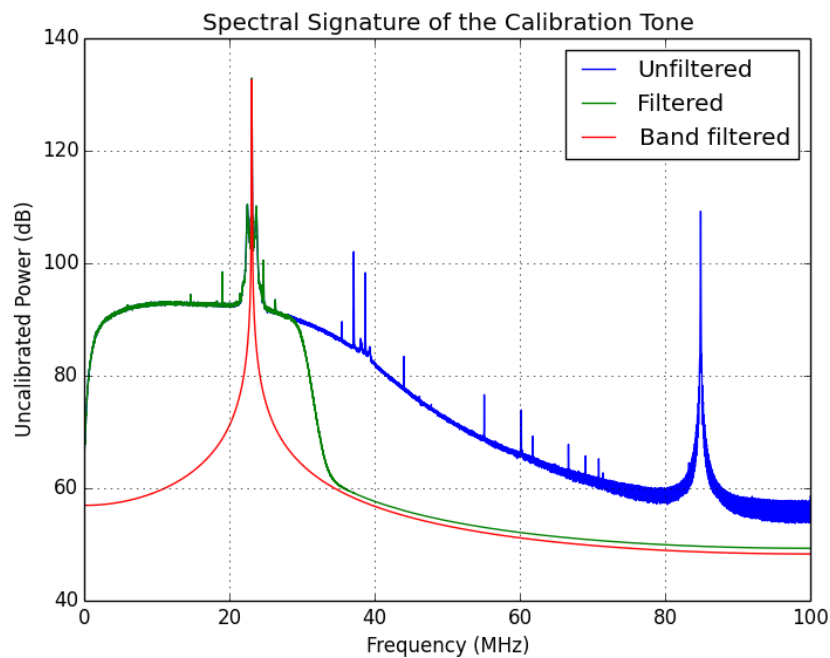


Figure 6: Spectrum of the received calibration signal.

The figure above shows the power spectrum of the received calibration tone. Although it is clearly not spectrally pure, we can filter out the unwanted signals to focus on the fundamental for calibration.

## Frequency Multiplier

To convert the L band signal to Ku band it is fed into a frequency multiplier whose topology is shown in Fig. 7. The frequency multiplier is a sextupler that is broken into a doubler followed by a tripler. The doubler is composed of a power splitter that is fed into a mixer to multiply the signal by itself. The tripler is composed of a bank of GALI-29+ amplifiers that drive the final amplifier into compression, generating odd-order harmonics of the fundamental. No harmonic-select filter is used, in part because the signal can be digitally filtered after reception, and because the input impedance of the transmitter itself will act as a filter against signals far from the desired harmonic.

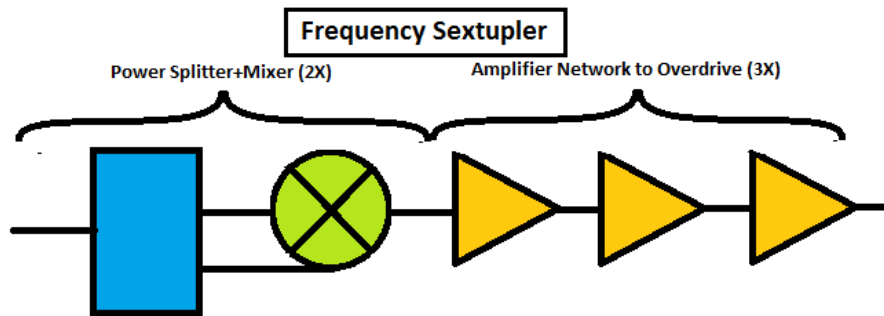


Figure 7: Block Diagram of the Frequency Multiplier



Figure 8: The frequency multiplier mounted on the transmit horn

### **Transmit Horn**

The transmit horn consists of a coaxial-cable-to-waveguide adapter, a quarter-wave monopole, and a circular microwave feed horn. The coaxial-to-waveguide adapter, shown bolted to the feed horn in Fig. 8, is a 1/2" diameter copper pipe end cap with a probe entrance hole drilled 6.5 mm from the back wall, which is approximately 1/4 wavelength. The outer conductor of a 0.085" diameter semi-rigid coaxial cable is soldered directly to the copper end piece with a 6.5 mm (1/4 wave) probe extending to the inside of the cavity. This is then bolted to the back of the feed horn. The feed horn is taken from a DirecTV dual feed LNB. Although it is a dual feed horn, only one feed is used. The front of the feed horn is shown in Fig. 9



Figure 9: Frontal view of the transmitting horn

### **2nd Stage Superheterodyne Receiver**

Typical Ku band satellite transponders have bandwidths between 27–50 MHz. The LNB horns output between 950–2150 MHz where several satellite channels are splayed across this 1 GHz band. The second-stage downconverter is a superheterodyne receiver, the schematic of which is shown in Fig. 10, that will take any 30 MHz channel from the 1 GHz band and convert the channel down to baseband to be digitized by the digitizer subsystem. The full downconverter consists of four identical chains where the mixers are driven by a common oscillator that is split to drive each of the chains. The full receiver is shown in Fig. 14. The individual components will be discussed in detail in the following sections.

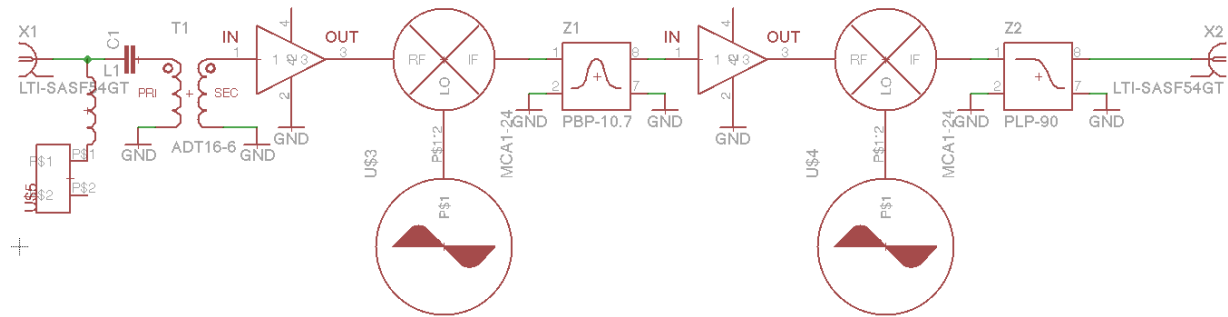


Figure 10: Schematics for a single channel of the 2nd stage downconverter.

### Bias-T

This allows us to provide phantom power to the LNB. The Bias-T consists of a 5.6 pF DC blocking capacitor, a 22 nH RF choke, and a 100 pF shunt capacitor. The basic schematic of the bias-T is shown in Fig. 11. It is basically a glorified high pass filter, where care is needed to make sure the high frequency behavior is not spoiled by the self-resonant frequencies of any of the constituent components.

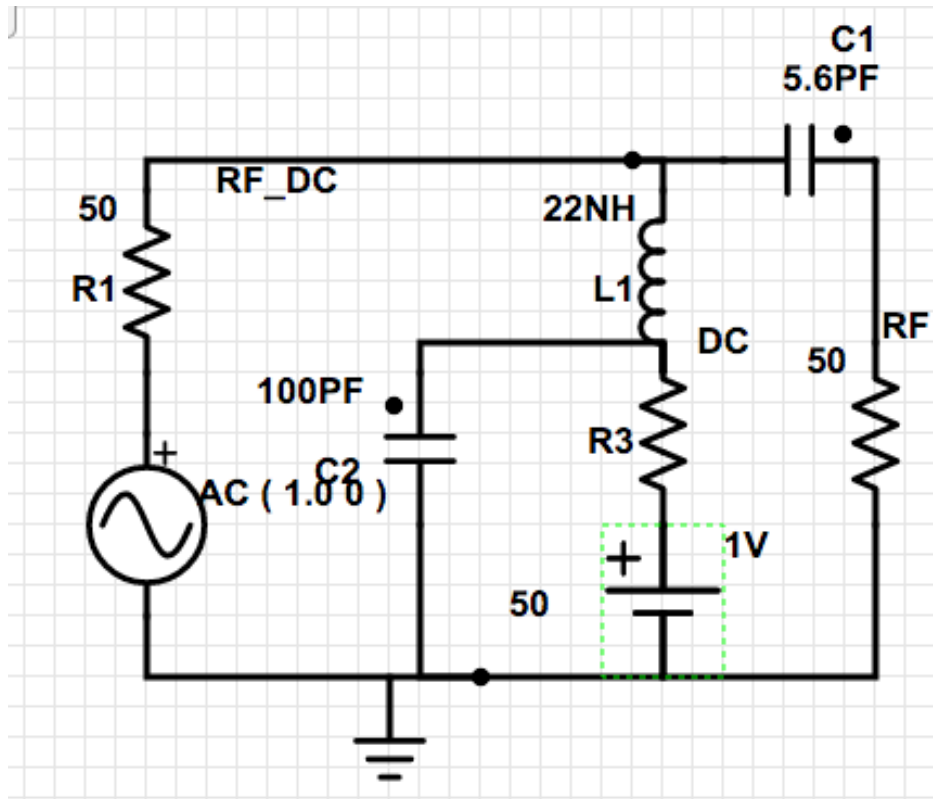


Figure 11: A SPICE Net of the bias-T

### Impedance Transformer

Commercial LNBS use 75  $\Omega$  transmission line, but most commercial test amplifiers and filters are designed with a 50  $\Omega$  characteristic impedance. Therefore an impedance-matching network must be included to prevent reflections and standing waves due to impedance mismatch. The TC1.5-1+ impedance transformer from Mini-Circuits was chosen because it has less than 1dB insertion loss over the band, which is phenomenal when compared to a matching pad which would have 4dB insertion loss.

### Amplifiers

The primary amplifier is a GALI-6+ monolithic amplifier from Mini-Circuits with 12 dB of gain in the band.

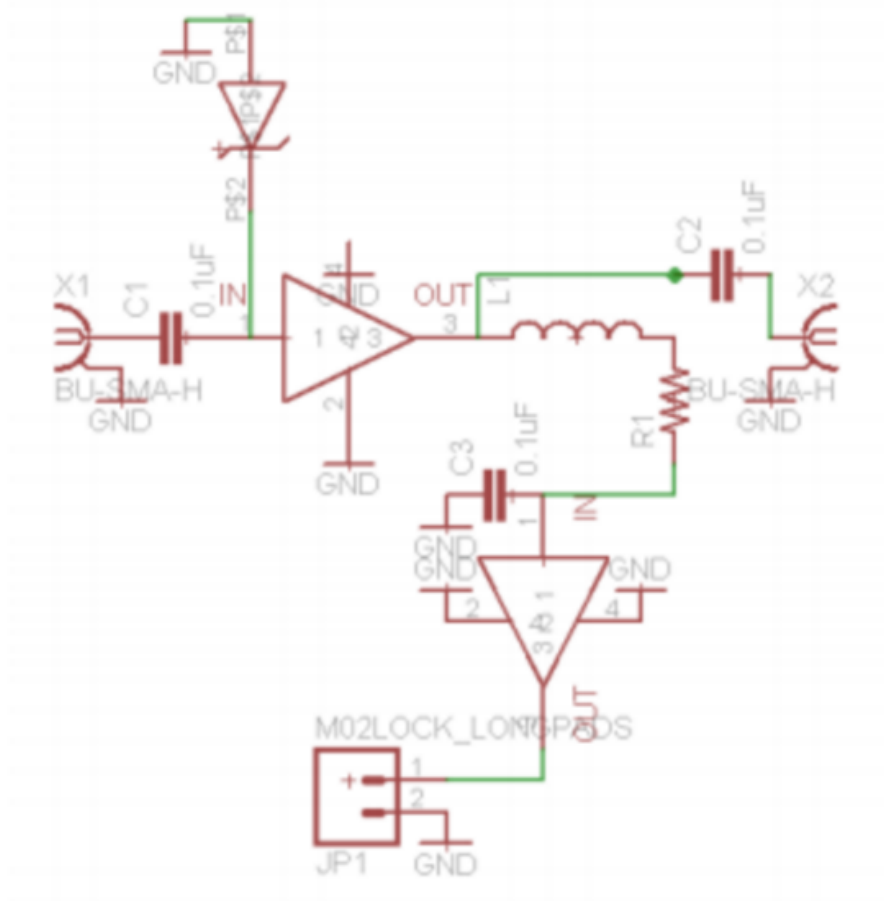


Figure 12: Electrical schematic of a GALI amplifier

The noise figure of the amplifier is negligible considering the fact that the LNB horn has such a small noise figure and 70 dB of gain. The Friis Noise Equation for cascaded devices is

$$F = F_1 + \frac{F_2 - 1}{G_1} + \frac{F_3 - 1}{G_1 G_2} + \dots + \frac{F_n - 1}{G_1 G_2 \dots G_{n-1}} \quad (9)$$

For a primary low noise amplifier with high gain this becomes

$$F = F_{\text{LNB}} + \frac{F_{\text{rest}}}{G_{\text{LNB}}} \quad (10)$$

The GALI-6+ has a noise figure of 4.5 dB, which makes the second term in the above equation on the order of  $10^{-6}$ , hence negligible. The IF Amplifier is a GALI-74+ amplifier from

Mini-Circuits and has 23 dB gain.

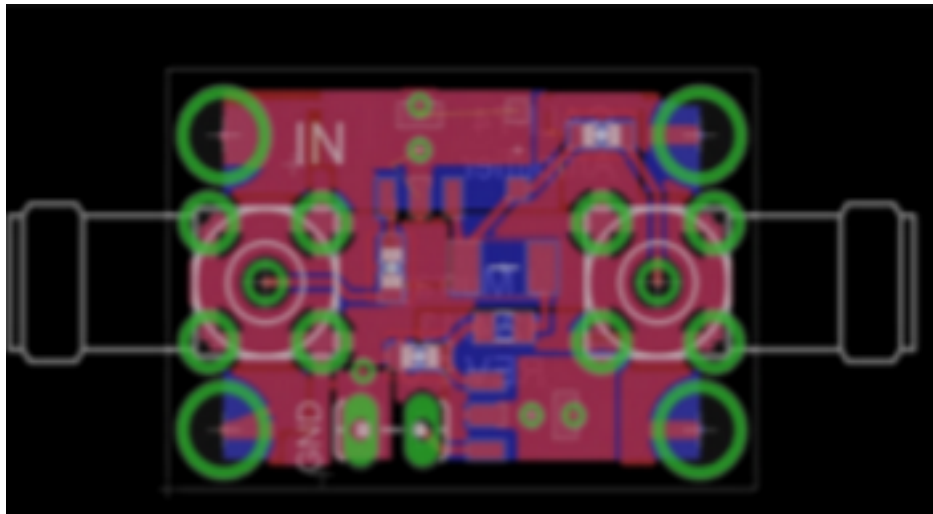


Figure 13: EAGLE software board file showing board layout

## Mixers

The primary mixer is an ADE-30+ commercial surface-mount mixer from Mini-Circuits which operates from 200–3000 MHz and has approximately 5 dB conversion loss when driven with a 7 dBm local oscillator (LO) signal. The secondary mixer is an ADE-1LH+, which operates from 0.5–500 MHz with a conversion loss of 5 dB when driven with a 10 dBm LO. Both local oscillators are laboratory signal generators that are operated in the frequency range of 720–1920 MHz and at 230 MHz respectively. The signal from each LO is split into 4 signals to feed each of the mixers in the 4 identical receiver chains.

## Digitizer Subsystem

Once the signal is brought to baseband it must be digitized for data analysis. For our digitizer we are using a Reprogrammable Open Architecture Computing Hardware (ROACH) board version 1.0 to control two dual-input 14-bit digitizers clocked at 200 MHz. This results in a 10/3 oversampling factor, which should increase our signal-to-noise ratio by the same factor. The

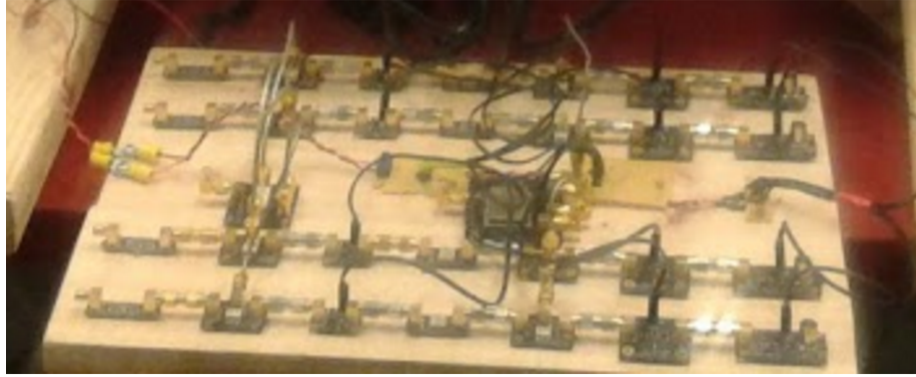


Figure 14: Full four channel superheterodyne receiver.

ROACH board will only be used for digitization and to ship the data to a general-purpose CPU.

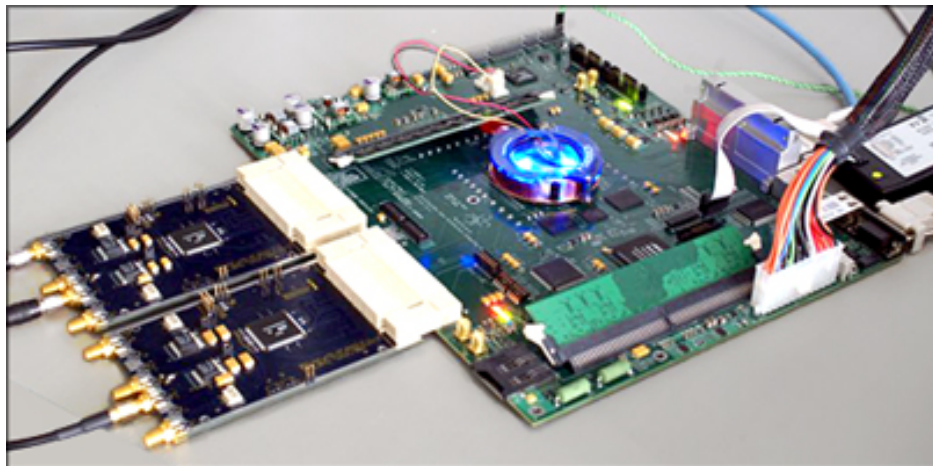


Figure 15: ROACH board in the configuration described

### **Data Analysis**

Once the data has been saved to disk, it will be analyzed to correct for the clock offsets and to steer the beams in real time. We want the system to be able calibrate to, search for and find multiple targets, form multiple spatial beams, and download data simultaneously from each target. For ease of initial testing the primary targets will be free-to-air geostationary satellites with the primary goal to be able to download data from multiple targets.

## Beamforming Computational Needs

For a simple delay and sum beamformer we can estimate the number of flops needed to beamform in real time. First one performs an FFT. Then each FFT needs to be multiplied by complex phase factors. Then all of the antennas need to be added together before finally performing an inverse FFT. The number of flops needed for the initial FFTs is

$$\text{FLOPS}_{FFT} = 5RN_{ant} \log(N_s) \quad (11)$$

where  $R$  is the sample rate,  $N_{ant}$  is the number of antennas, and  $N_s$  is the number of samples in the computation. It is important to note that these initial FFTs do not scale with the number of beams. For  $N$  real points into the FFT, we get  $N/2$  complex points out. Each of these then needs to be multiplied by a complex phase factor, where each complex multiply is 6 floating point multiplies. This leads the number of FLOPS per beam to be

$$\text{FLOPS}_\phi = 3RN_{ant} \quad (12)$$

To form the beam the signals must then be added together. The number of FLOPS per beam is

$$\text{FLOPS}_\Sigma = R(N_{ant} - 1) \quad (13)$$

Finally we must apply an inverse FFT on the signal to get the final signal. The inverse FFT can have fewer channels than the initial FFT if the required bandwidth is less than the input bandwidth. The number of FLOPS per beam is

$$\text{FLOPS}_{FFT^{-1}} = 5R \log(N_s) \quad (14)$$

Now the total number FLOPS can be calculated as

$$\text{FLOPS} = \text{FLOPS}_{FFT} + N_B (\text{FLOPS}_\phi + \text{FLOPS}_\Sigma + \text{FLOPS}_{FFT^{-1}}) \quad (15)$$

where  $N_B$  is the number of beams. Using the above, for a 4-element array with 200 MHz samplers, a  $2^{20}$  channel FFT and 2 spatial beams, the necessary computational power for simple delay-and-sum beamforming is 138 GFLOPs.

### Calibration and Beamforming Computational Needs

Once the calibration coefficients have been determined from a calibration dataset, the calibration requires  $N$  complex multiplications on real data, an FFT,  $N/2$  more complex multiplications, and then an inverse FFT. So the number of flops for the initial multiplications is

$$\text{FLOPS}_{\Delta f} = 2R(N_{ant} - 1) \quad (16)$$

The number of flops for the FFT are

$$\text{FLOPS}_{FFT} = 5R(N_{ant} - 1) \log(N_s) \quad (17)$$

The number of flops for the time calibration is

$$\text{FLOPS}_{\Delta t} = 3R(N_{ant} - 1) \quad (18)$$

Now the number of flops need for the inverse FFTs is

$$\text{FLOPS}_{FFT^{-1}} = 5R(N_{ant} - 1) \log(N_s) \quad (19)$$

and now the total flops are

$$\text{FLOPS} = \text{FLOPS}_{\Delta f} + \text{FLOPS}_{FFT} + \text{FLOPS}_{\Delta t} + \text{FLOPS}_{FFT^{-1}} \quad (20)$$

For  $2^{20}$  frequency bins the number of flops necessary to perform the corrections in real time is 135 GFLOPS.

Now the naive way to find the total flops, both calibrating and beamforming in real time, would be to add both flops, which gives 273 GFLOPS. We can, however, take advantage of the similarity between the calculations to combine steps from both processes into a single step. The revised combined necessary flops is

$$\text{FLOPS}_{\Delta f} = 2R(N_{ant} - 1) \quad (21)$$

which performs the frequency shift of the uncalibrated data. Now we take an FFT of the data.

$$\text{FLOPS}_{FFT} = 5RN_{ant} \log(N_s) \quad (22)$$

At this point, there exist two  $\Delta t$  values: one for the calibration and another for the beam steering. Instead of applying each separately we can perform  $3N_B$  operations (additions) to combine the separate  $\Delta t$  values into single values. The next step would be to multiply these, which takes

$$\text{FLOPS}_{\Delta t \& \phi} = 3RN_{ant} \quad (23)$$

per beam. Then the flops per beam for summation is

$$\text{FLOPS}_{\Sigma} = (N_{ant} - 1)R \quad (24)$$

and the final inverse FFT per beam costs

$$\text{FLOPS}_{FFT^{-1}} = 5R \log(N_s) \quad (25)$$

The total flops for calibration and beam steering is

$$\text{FLOPS} = \text{FLOPS}_{\Delta f} + \text{FLOPS}_{FFT} + N_B(\text{FLOPS}_{\Delta t \& \phi} + \text{FLOPS}_{\Sigma} + \text{FLOPS}_{FFT^{-1}}) \quad (26)$$

which for  $N_s = 2^{20}$  and  $N_B = 2$  gives 227.2 GFLOPs. This is something that can easily be accomplished with an \$200–500 GPU like the NVIDIA Quadro 4000.

## CHAPTER III

### BEAMFORMING

Let's consider a linear array of antennas like that shown in Fig. 16

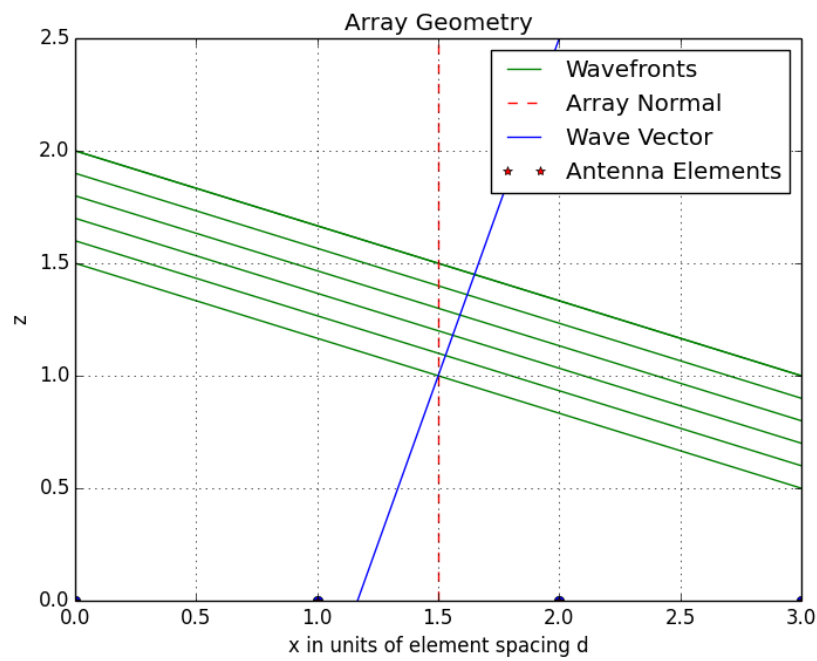


Figure 16: Geometry of a uniformly spaced linear array

The Array Factor measures the sensitivity of the array to waves from a given direction, and is defined as

$$AF = \sum_{n=0}^{N-1} w_n e^{-i\vec{k} \cdot \vec{r}_n} \quad (27)$$

where  $\vec{k}$  is the wave vector,  $\vec{r}_n$  is a vector pointing to the  $n^{\text{th}}$  antenna,  $w_n$  is a complex weight, and  $N$  is the total number of elements. For an evenly spaced array we can steer the beam of the array

in the direction of  $\theta_d$  using the weights

$$w_n = e^{iknd \sin \theta_d} \quad (28)$$

where  $\theta_d$  is measured from the array normal. The position vector is given by

$$\vec{r}_n = (nd, 0, 0) \quad (29)$$

If we plug these back into the Array Factor we obtain

$$\begin{aligned} AF &= \sum_{n=0}^{N-1} e^{iknd(\sin(\theta_d) - \sin(\theta))} \\ &= \sum_{n=0}^{N-1} \left( e^{ikd(\sin(\theta_d) - \sin(\theta))} \right)^n \\ &= \frac{1 - e^{ikNd(\sin(\theta_d) - \sin(\theta))}}{1 - e^{ikd(\sin(\theta_d) - \sin(\theta))}} \end{aligned} \quad (30)$$

where  $\theta$  is the angle off of the z-axis. If we now take the absolute value of array factor we obtain

$$|AF| = \frac{\sin(kNd(\sin \theta_d - \sin \theta)/2)}{\sin(kd(\sin \theta_d - \sin \theta)/2)} \quad (31)$$

For our array we have  $d = 10\text{cm}$  and  $f = 10\text{GHz}$ . The array factor is plotted in Fig. 17 for  $\theta_d = 0$ . As expected the main beam is pointed at zenith but there are also several grating lobes of equal amplitude to the main beam. Grating lobes are expected for inter-element spacing greater than  $\lambda/2$ , whereas our spacing is about  $4\lambda$ . This is due to the physical size of the constituent array elements. In Fig. 19 we see element factor, which is the beam pattern of an individual element, is highly directive. The array response in Fig. 20 shows how the the directivity of the element factor significantly reduces grating lobe levels. In general, phased arrays would prefer to have low-directivity elements, because the higher the directivity, the more attenuated the array factor becomes at large scan angles. For our element factor, the half-power beam width would limit us to about a  $\pm 9$  degree scan angle limit. The major limit on our scanning angle is not the element factor directivity, but the inter-element spacing. In Fig. 21 we see one of the grating lobes starting

to creep up as the array is steered to 5 degrees. By the time we reach 7 degrees as shown in Fig. 22 a grating lobe has already overtaken the main lobe in relative amplitude. This limits our scanning to about  $\pm 7$  degrees. This is fine, though, because as shown in Appendix A, there as many as 8-10 possible targets in an 14 degree scan window.

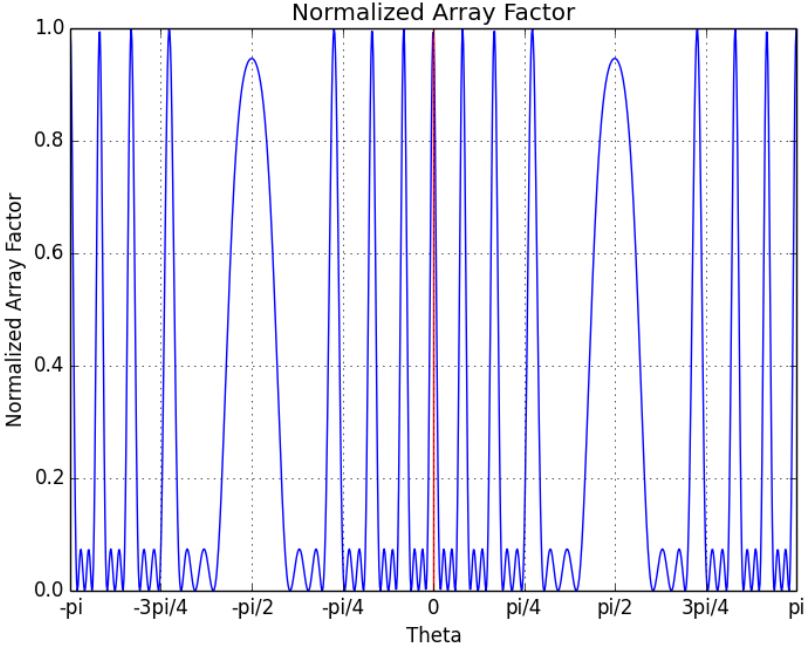


Figure 17: Array factor for our array

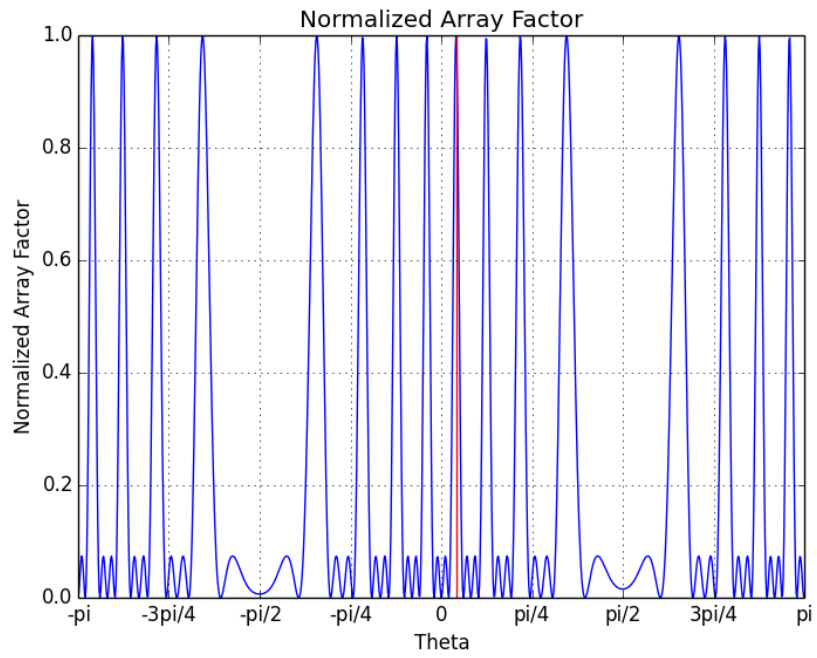


Figure 18: Array factor steered toward 7 degrees off zenith

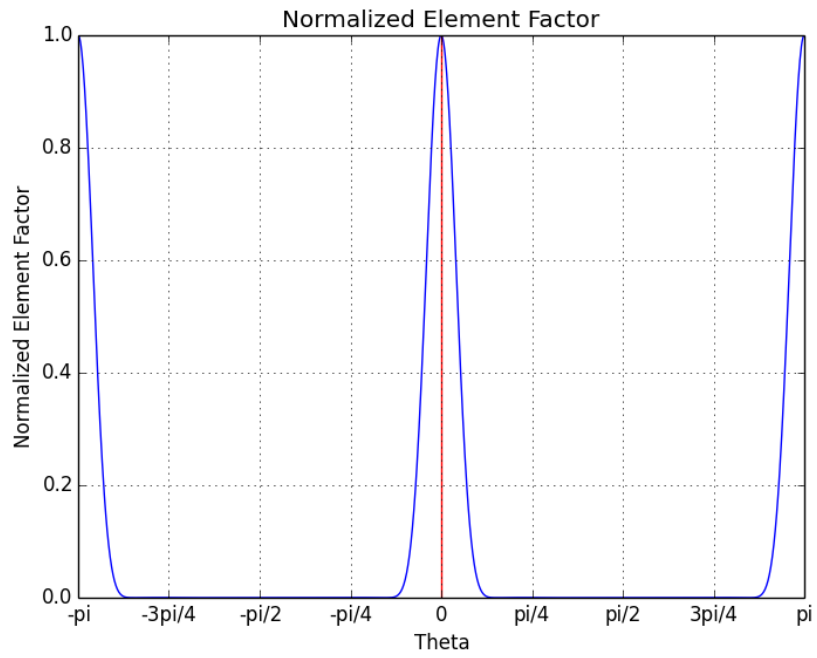


Figure 19: The element factor modeled by an Airy disk

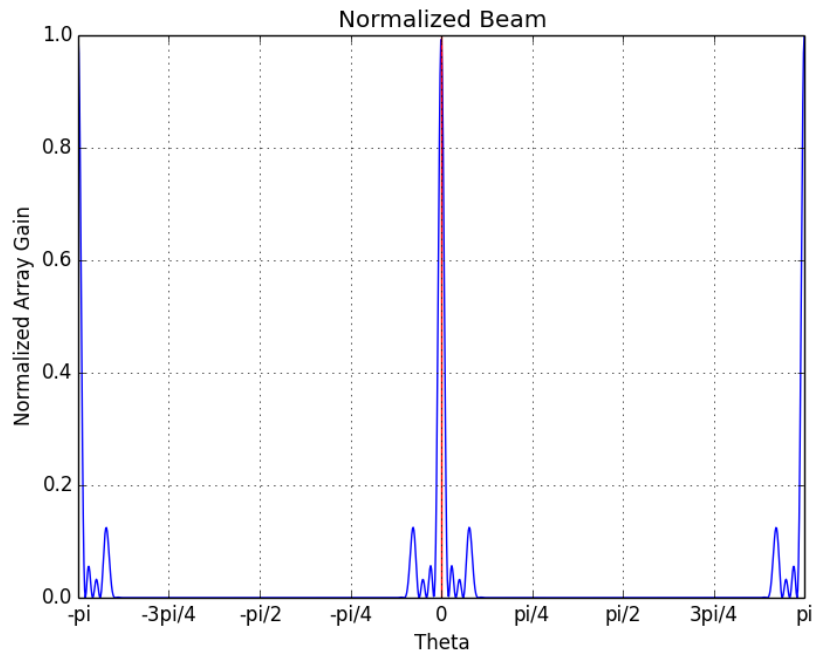


Figure 20: Normalized array response at zenith

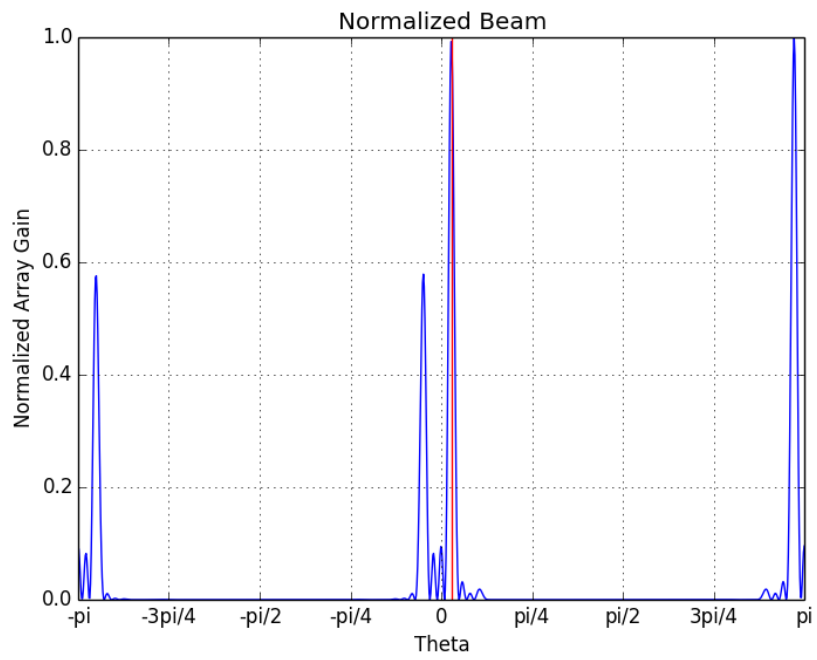


Figure 21: Array response at 5 degrees

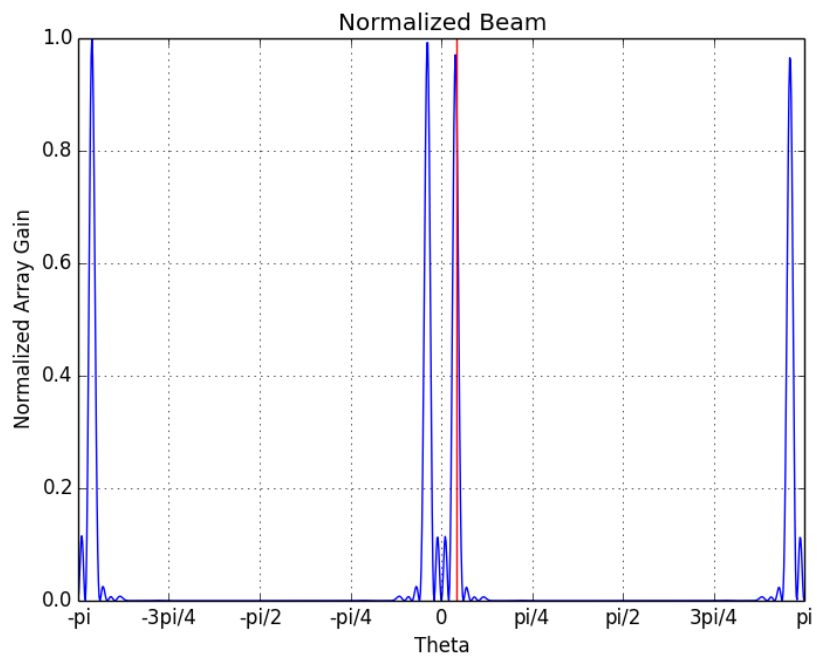


Figure 22: Array response at 7 degrees: Steering angle is grating lobe limited

## CHAPTER IV

### CALIBRATION

The ability of the array to beamform will only be as good as the calibration of the array. Before any beamforming can take place a calibration dataset must be taken in the configuration shown in Fig. 23. The transmit antenna is placed in the far field of the array where the far field is defined as satisfying all of the following

$$\begin{aligned} R &> \frac{2D^2}{\lambda} \\ R &\gg D \\ R &\gg \lambda \end{aligned} \tag{32}$$

where  $R$  is the distance from the array,  $D$  is the maximum linear dimension of the array, and  $\lambda$  is the wavelength.



Figure 23: Calibration Test Set Up

## Frequency and Phase Calibration

The frequency calibration consists of a coarse calibration using FFTs to roughly determine the frequency of the incoming calibration tone, and a refined calibration using phase-time calculations for each signal. To begin the rough calibration, we remove the DC offset from each signal. We then calculate the power spectrum of each signal and find the maximum bin of the power. Then we place a window around this bin and perform a cubic spline interpolation to more exactly determine the frequencies of the signals. Once the frequencies are found we declare one to be the "reference horn" and find the frequency differences,  $\Delta f$ , between the reference and the other horns. We can then multiply the time series of each horn by a factor  $e^{i2\pi\Delta f t}$  corresponding to their difference frequency to shift them to the reference frequency. The result of such a shift is shown in Fig. 24.

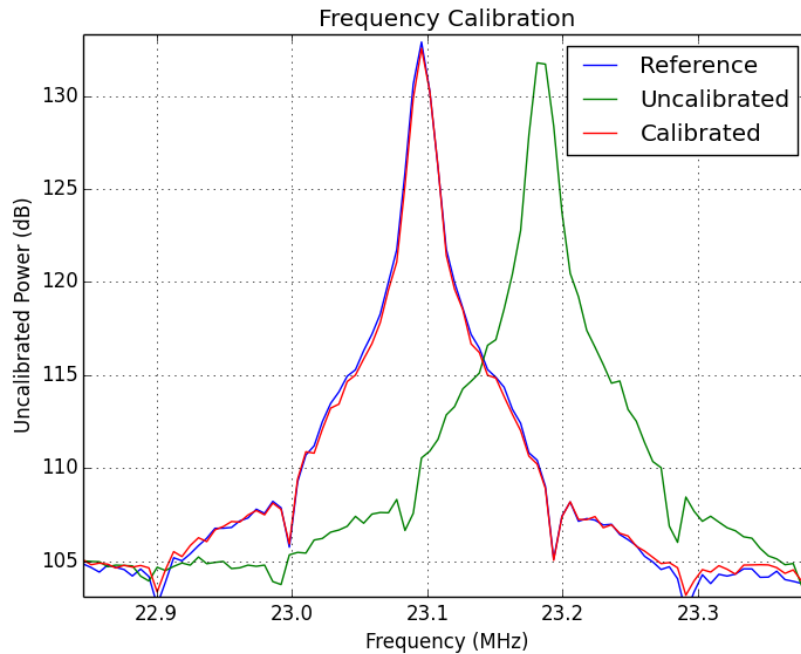


Figure 24: Results of a frequency calibration

If we look back at Eq. 8 we recognize how important a good frequency match is. It would pay to examine the bounds on the error associated with the frequency determinations. If we

took the frequency straight from the maximum bin, our uncertainty would scale linearly with the resolution bandwidth. That is to say,

$$\max |\varepsilon| \leq \frac{R}{2N} \quad (33)$$

where  $R$  is the sampling rate,  $\varepsilon$  is the error, and  $N$  is the number of time samples used for calibration. For a polynomial spline interpolation the error bound has the follow form

$$\max_{x \in [a,b]} |f(x) - p_n(x)| \leq \left( \frac{b-a}{n} \right)^{n+1} \frac{1}{4n+1} \max_{x \in [a,b]} |f^{(n+1)}(x)| \quad (34)$$

where  $f(x)$  is the function being fit,  $p_n(x)$  is an  $n$  degree polynomial, and  $[a, b]$  is the interval over which the interpolation is done. For a cubic spline,  $n = 3$ , and the interval goes over the center frequency  $\pm 50$  bins. We can assume the function we are trying to fit is a sinc function, because the Fourier transform of a windowed sinusoid is a sinc function, whose width is inversely proportional to the width of the window. In examining Eq. 34, we notice that not only does  $b - a$  depend on the number of samples, but the argument of  $f(x)$  does as well, which leads to an additional  $1/N^4$  in the error function. The errors for both frequency estimation methods are shown in Fig. 25.

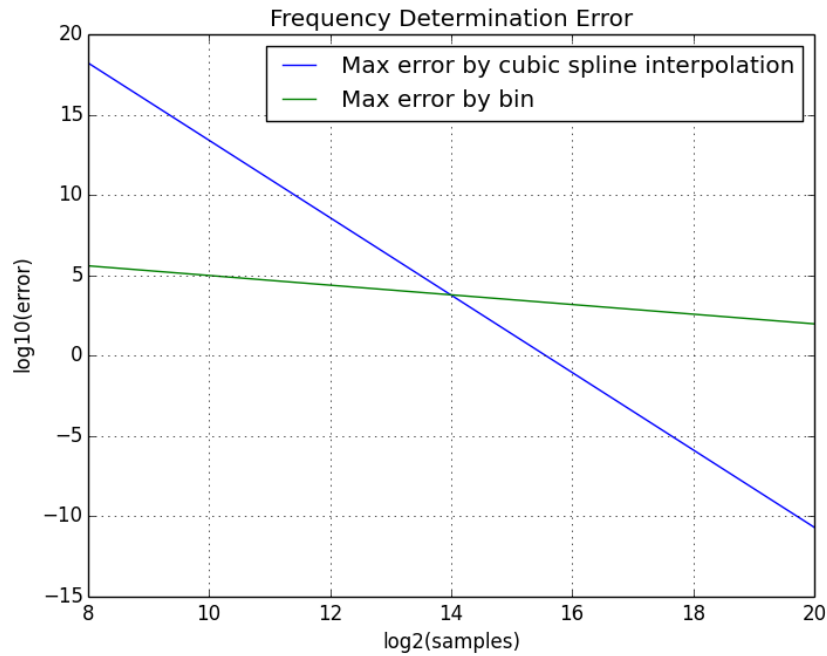


Figure 25: Error of frequency estimation

Once the coarse frequency calibration has been performed we then calculate the phase versus time of each horn by taking small 512-sample FFTs and pulling the phase from the real and imaginary parts of the maximum bin. This re-samples our data to about 390 kHz. Since our initial frequency differences can be on the order of hundreds of kilohertz, the coarse calibration is necessary to make sure that the phase-time calculations don't become subject to aliasing. To determine the frequency differences we make a linear least-squares fit of the differences of the phases versus time and use the determined slope to perform the fine frequency calibration. A plot of the phase-time calculation is shown in Fig. 26.

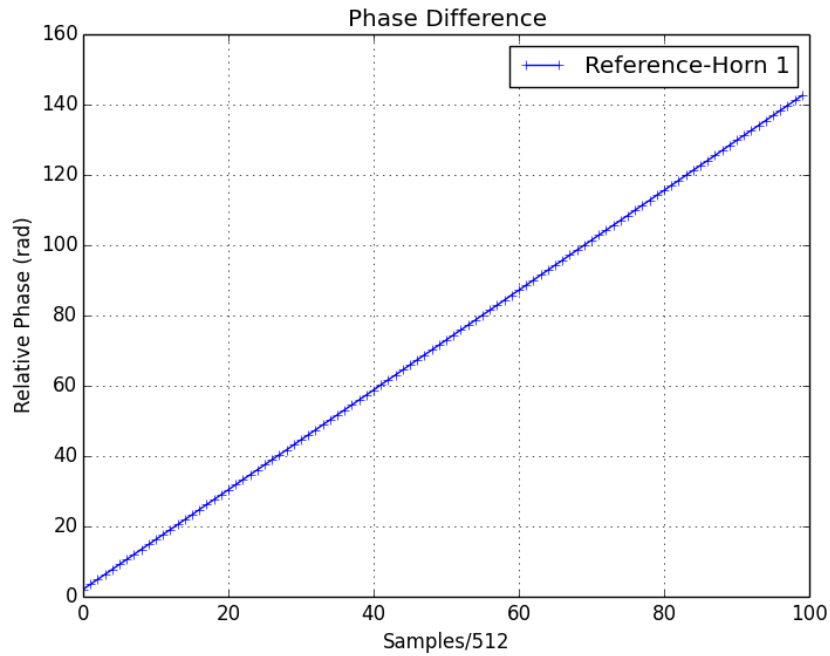


Figure 26: Phase-time plot of an individual horn

Once the frequency differences of the horns are all calibrated, one can again compute the phase of each of the signals. Using the reference horn as the model, the phase differences between horns can be calculated by taking the mean of the phase residuals. One can then divide the resulting phase difference of the signal by the calibration frequency to extract the time difference,  $\Delta t$ , between each horn and the reference. Once  $\Delta t$  is found, the phase shift is performed by multiplying the Fourier transform of the data by a frequency-dependent factor  $e^{i2\pi f\Delta t}$  and applying the inverse Fourier transform. A plot of the typical post-phase-calibration residuals is shown in Fig. 27.

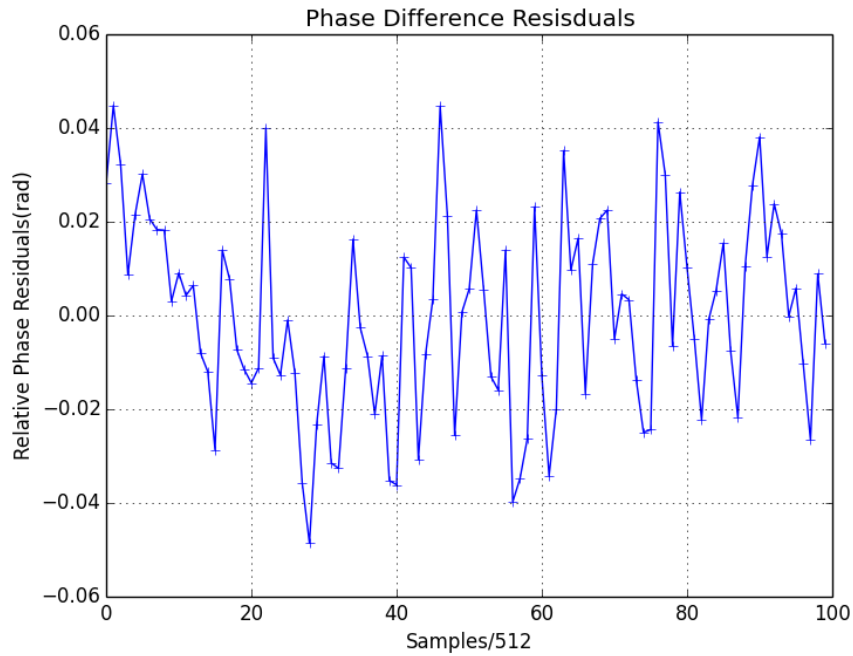


Figure 27: Phase residuals for calibrated data

It should be noted that the phase shift is performed making the assumption that there is a linear relationship between phase and frequency within the band, which should be a valid approximation. The filters used in the receiver system were chosen to have a linear phase response for this exact reason. The typical results of the frequency and phase calibration algorithms outlined above are shown in Fig. 28 and Fig. 29.

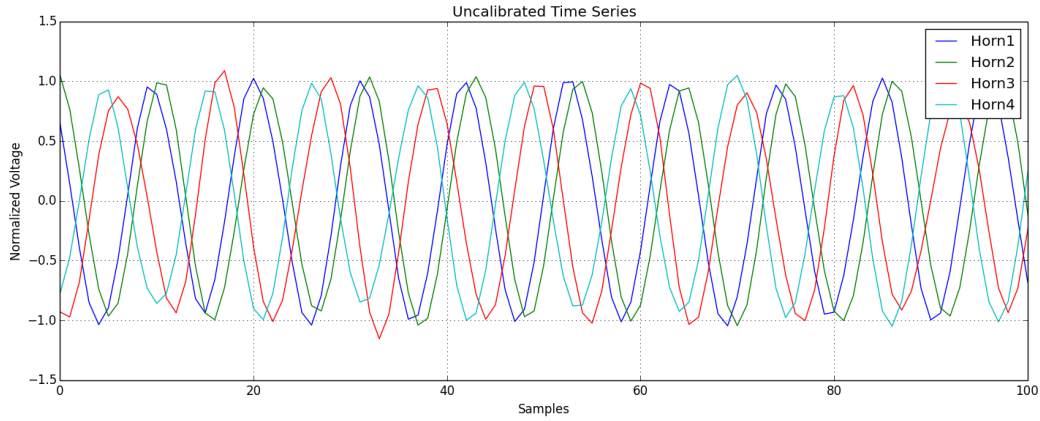


Figure 28: Uncalibrated test data

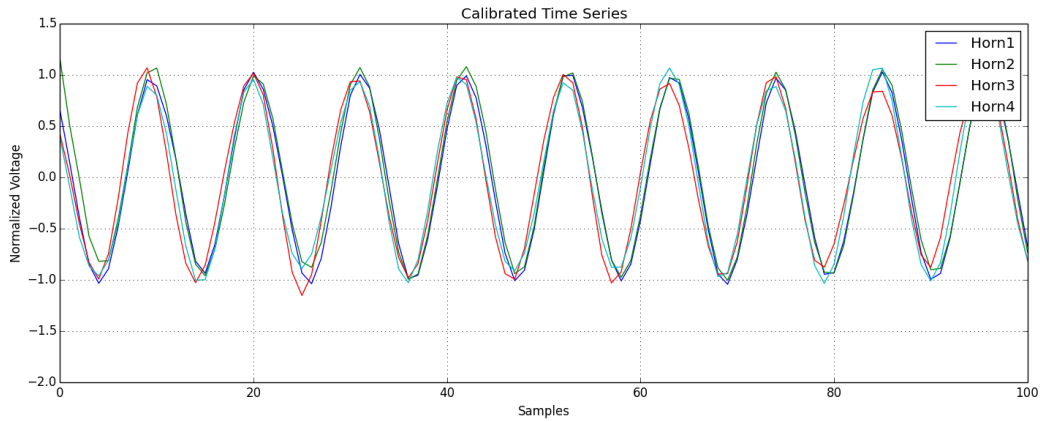


Figure 29: Calibrated test data

### Coherence Time

As was mentioned previously, the frequency matching between antenna elements is crucial. Assuming that the frequencies of the oscillators in the horns are stable, the precision of the frequency match dictates the time scale over which the signals will be coherent. To quantify this we can define the coherence time as the time it takes for the correlation coefficient of two signals of slightly different frequencies to drop to one half. Using this definition we can write

$$\tau = \frac{1}{4\delta f} \quad (35)$$

where  $\tau$  is the coherence time and  $\delta f$  is the error in frequency. That is, the coherence time is one quarter of the period of the frequency error. The coherence time sets a limit on the length of the Fourier transforms that be performed on the data:

$$\frac{N}{R} \leq \tau \quad (36)$$

where  $R$  is the sampling rate and  $N$  is the number of samples. This inequality can be used in conjunction with Fig. 25 to determine the length of the calibration dataset to produce a certain frequency resolution in the data analysis. Once the frequency difference is found, it can be used for all subsequent calibrations. Then the phase differences can be calculated and calibrated at each time interval, as long as that time interval is less than the coherence time.

## CHAPTER V

### DATA

The data is shipped from the ROACH board to the computing CPU in network packets of 8192 bytes. Due to a limitation of the current data taking system, there is a buffer overflow when reading the data from the network socket after 25 data packets. After 25 frames, packets would be dropped randomly, resulting in phases like those shown in Fig. 30. The same effect can be seen in the raw time series in Fig. 31, where two in-phase signals of the same frequency abruptly change phase due to missing chunks of time. This means we were limited to a total of 51,200 contiguous data samples at a time for the following calculations.

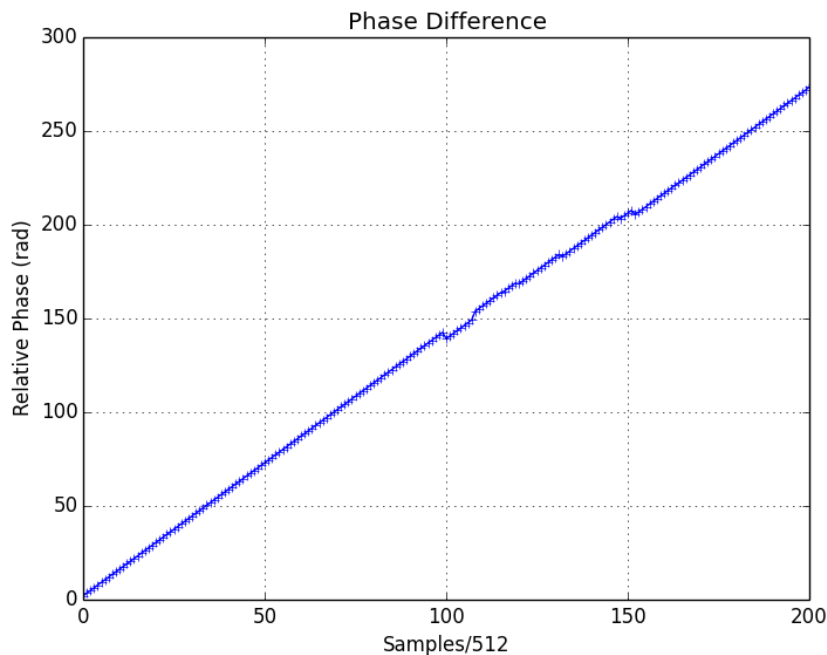


Figure 30: Phase jumps from dropped data packets

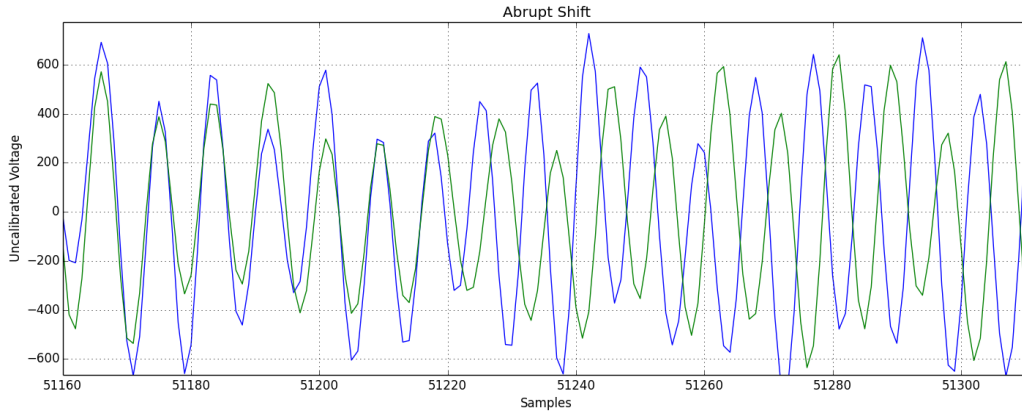


Figure 31: Raw time series showing the abrupt phase shift

Even with this limitation we were able to show that we achieve coherent addition of the signals in our array. Furthermore, we have shown that the coherence time of our calibration is greater than the time needed to perform the corrections, and that the frequencies of the oscillators in each of the horns is stable over long time intervals. We have also shown that we can beamform and steer the resulting beam, even placing the calibration signal into a beam null.

### Array Gain

After calibration we should see a factor of sixteen increase in power from the array. Since uncorrelated noise power should only increase by a factor of four, we should see an increase in SNR of four. We can see in Fig. 32 that the normalized time series add to an increase of four in voltage, which is a factor of sixteen in power.

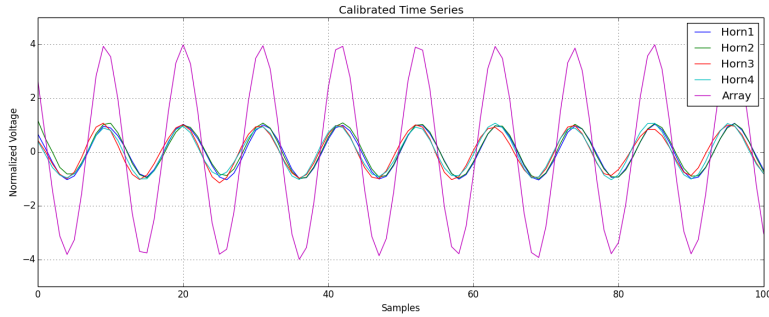


Figure 32: Time series signal addition

In Fig. 33 we see the power spectra of individual horns plotted on top of that of the full array. When we compare the blue curve that to that of Horn 1, we can see the expected 6dB increase in SNR.

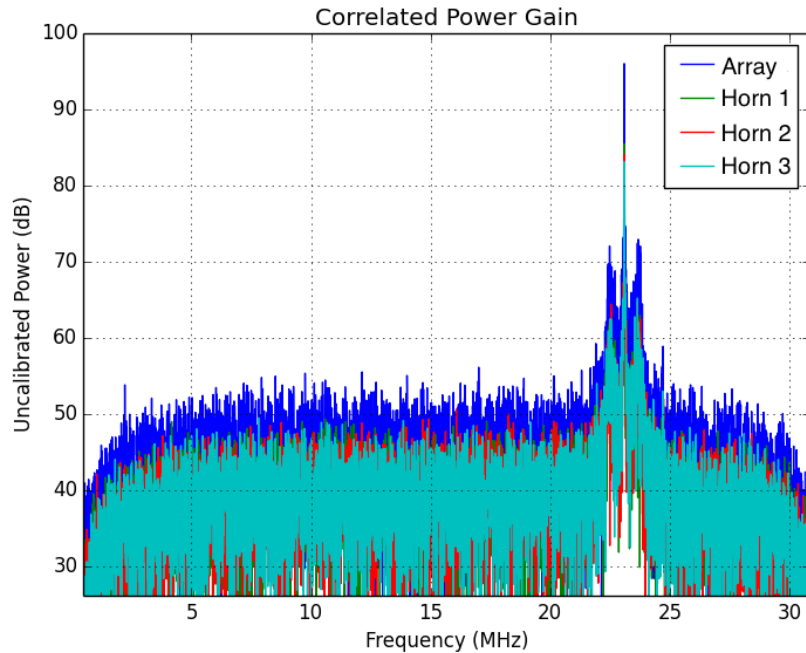


Figure 33: Plot showing coherent addition of signals

In the calibration section we mentioned that the phase calibration made the assumption that the phase-frequency relationship of the signal was linear. To test whether the calibration was valid outside of the vicinity of the calibration tone, two datasets were taken: one with just the

calibration tone, another with the calibration tone and a broadband noise source. In the first case the noise in each horn should be uncorrelated, resulting in coherence only at the frequency of the tone. In the second case the noise should be correlated across horns resulting in 12dB gain across the band. We see this in Fig. 34 where we have subtracted the logarithmic power of the reference horn from that of the entire array. In the case of no coherent noise the signal difference falls off away from the calibration frequency. In the case of coherent noise we have a 12dB increase across the band.

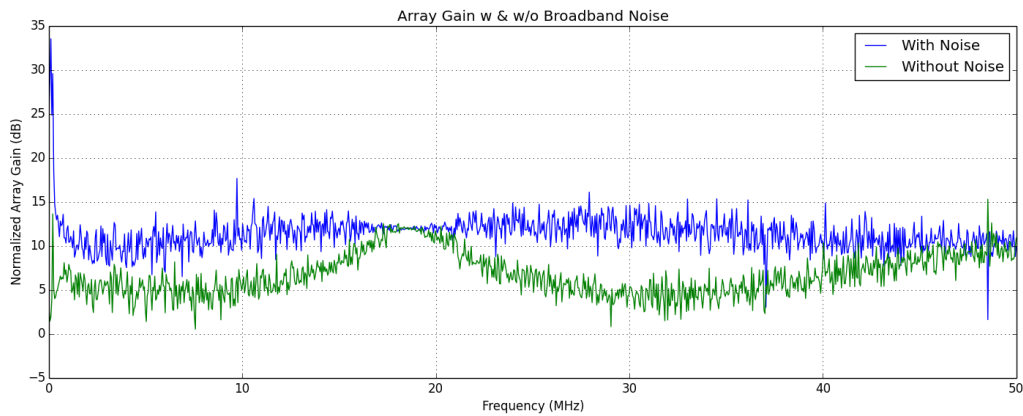


Figure 34: Gain of the array with and without broadband noise

### Coherence Time

Since we were limited in the total length of contiguous data we could take, we could not determine the total coherence time of our calibration. We did, however, show that the coherence time is greater than the time needed for the calibration and beamforming. Furthermore, we showed that the frequencies of the oscillators are stable on the order of at least ten minutes. This was shown by taking several datasets spaced tens of seconds apart over the course of ten minutes. The first of the datasets was used to determine the frequency offsets and the initial phase offsets, the results of which are shown in the table below, where Horn 2 is the reference. The same frequency calibration data was then used to calibrate the subsequent datasets where only the phase offsets needed to be computed. Average power of the signals is shown for the data over the

course of the ten minutes in Fig. 35, where not only does the calibration work over a single dataset, but it works on all of the datasets, showing a factor of sixteen increase average power over the normalized reference.

	$\Delta f$ (Hz)	$\Delta t$ (ns)
Horn 1	-88434.84	23.65
Horn 2	0	0
Horn 3	-6530.40	40.0
Horn 4	96551.61	26.55

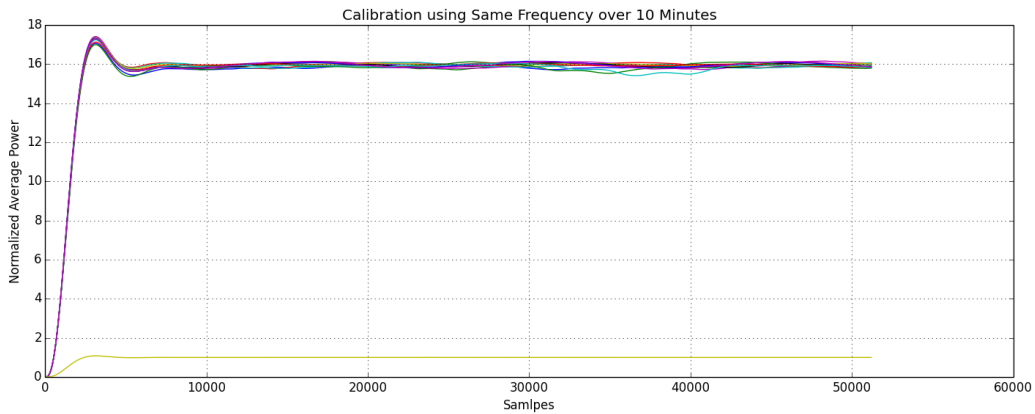


Figure 35: Average power of several datasets using the same calibration data

### Beamforming

One of the primary advantages of the phased array is the ability to electronically steer the beam of the array. One can think of the initial frequency-phase calibration as steering the beam to the normal axis of the array. Once this is done, one can begin to add the appropriate offsets to each horn to begin steering the array away from the normal axis. In Fig. 36 we have predicted the power entering the array as a function of steering angle and plotted it alongside the measured power.

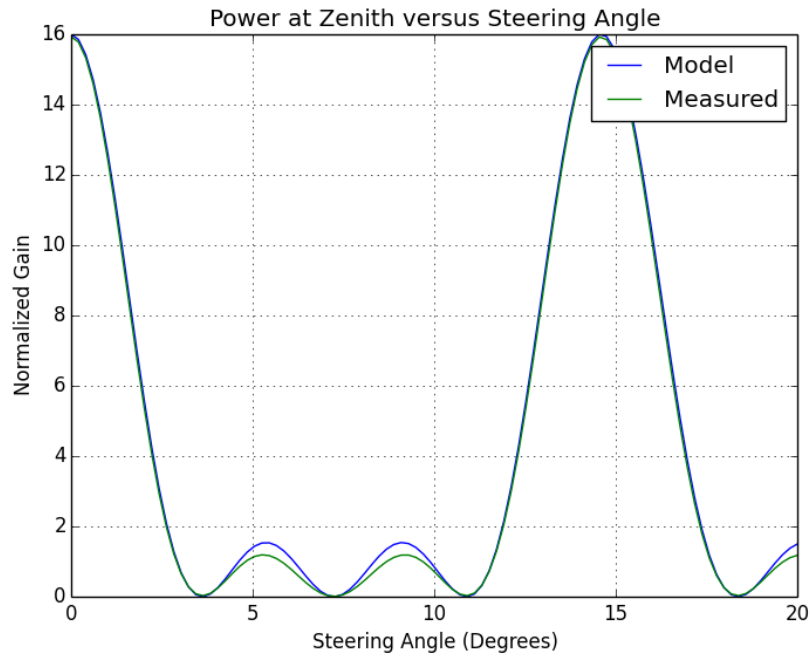


Figure 36: Power versus steering angle

Here we see that the measured power lines up pretty well with the model at the main peaks and nulls. To see the the level of attenuation in the nulls of the array, we plot the power on a log scale as shown in Fig. 37, where the main null is shown to attenuate by 30 dB and the secondary null attenuates by 40 dB.



Figure 37: Beam null effectiveness

## CHAPTER VI

### CONCLUSIONS

We have shown that we can create a phased array using cheap non-synchronized LNBS to achieve broadband coherent gain. We have demonstrated that our calibration techniques provide for a coherence time that is long enough to perform phase calibrations and beamsteering. We have shown that once the frequency differences have been determined, the oscillators in each horn are stable over long timescales. We have been able to steer the array once calibrated and place the source in a beam null. In the future we would like to be able to demonstrate steering the array onto a secondary source, and eventually onto a satellite in order to download data. The design that we have outlined has the potential to be a low-cost, highly functional alternative to traditional mechanical dish tracking of space assets. Not only that, but these methods can also be applied to potentially any set of non-synchronous antennas such as software-defined radio antennas. One could potentially use any number of small independent radios to perform beamforming and interferometric measurements, with the added benefit of supreme reconfigurability. This could not only impact the field of telecommunications but also astronomy, amateur radio, and any field where the same technique could be extrapolated to general sensor arrays.

## REFERENCES

- ATIS Telecom Glossary. (n.d.). Retrieved March 16, 2016, from <http://www.atis.org/glossary/definition.aspx?id=2816>
- Braun, K. F. (1909). Electrical oscillations and wireless telegraphy. Nobel Lecture, December, 11(1909), 226-245.
- Swords, S. S. (1986). Technical History of the Beginnings of Radar. London: IEE/Peter Peregrinus.
- AEGIS weapon system MK-7. (n.d.). Retrieved March 17, 2016, from <http://web.archive.org/web/20060701055247/http://www.janes.com/defence/navalforces/news/misc/aegis010425.shtml>
- Mumford, W. W. (1949). A BroadBand Microwave Noise Source. Bell System Technical Journal, 28(4), 608-618.
- Rogers, A. (2007). Tests of compact fluorescent lamp as microwave sources. VSRT and MOSAIC Memo Series.
- Rogers, A. (2006). Preliminary concept for VSRT image processing. VSRT and MOSAIC Memo Series.
- Pozar, D. (2012). Microwave engineering. Hoboken, NJ: Wiley.
- Chen, H. C., Lin, T. H., Kung, H. T., Lin, C. K., and Gwon, Y. (2012). Determining RF angle of arrival using COTS antenna arrays: a field evaluation. In MILITARY COMMUNICATIONS CONFERENCE, 2012-MILCOM 2012 (pp. 1-6). IEEE.
- Mailloux, R. J. (1994). Phased array antenna handbook. Boston, MA: Artech House, 1994.
- Sarkar, T., & NetLibrary, I. (2006). History of wireless. Hoboken, N.J: Wiley-Interscience.
- Friis, H. T. and Feldman, C. B. (1937), A Multiple Unit Steerable Antenna for Short-Wave Reception. Bell System Technical Journal, 16: 337419. doi: 10.1002/j.1538-7305.1937.tb00425.x
- G. Marconi, "Directive Antenna," Proc. Royal Soc., London, 77A, p. 413,1906.
- H. Friis "A New Directional Receiving System," IRE Proc., Vol.13, No. 6, Dec. 1925, pp.685-708
- E. Bruce and A. C. Beck, "Experiments with directivity steering for fading reduction," Proc. I.R.E., Vol. 22, pp. 45-78, Jan 1934.

## APPENDIX

## APPENDIX

### VISIBLE GEOSTATIONARY SATELLITES

Satellite Name	Location	EIRP in Brownsville (dBW @ Ku Band)
Galaxy 3C	95 W	49.1
Galaxy 17	91 W	50.4
Galaxy 18	123 W	50.8
Galaxy 19	97 W	48.5
Galaxy 25	93 W	50.0
Galaxy 28	89 W	50.0
Horizons 1	127 W	48.0
Intelsat 23	307 E	51.6
Direct TV 92 (Conus Beam)	101 W	56.1
Skyterra 1 (TKU1 Beam)	101 W	50.8
Direct TV 15 (Conus Beam)	103 W	55.0
AMC 15	105 W	50.7
Echostar 11	110 W	52.2
Direct TV 5	110 W	50.0
Echostar 10	110 W	59.2
Eutelsat 113 West A	113 W	50.0
Eutelsat 115 West A	115 W	51.0
Eutelsat 117 West A	117 W	50.0
Echostar 14	119 W	53.8
Echostar 17	119 W	53.0

Direct TV 7s	119 W	61.1
AMC 21	125 W	50.0
Ciel 2	129 W	55.7

## BIOGRAPHICAL SKETCH

James Isaiah Murray is currently a researcher at the University of Texas Rio Grande Valley(UTRGV) and works in the Center for Advanced Radio Astronomy(CARA). Within the Center, Murray is an Arecibo Remote Command Center(ARCC) Scholar, conducts research in the Spacecraft Tracking and Astronomical Research into Gigahertz Astrophysical Transient Emission(STARGATE) program, and as Head Technician for the Center for Advanced Radio Astronomy Multipurpose Electronics Laboratory(CARAMEL), manages the Center's electronics lab. He earned a B.S. in Physics with a focus in Radio Astrophysics from the University of Texas at Brownsville(UTB) in 2014. In 2016 Murray earned an M.S. in Physics from UTRGV for research in phased array technology.

James completed an internships at the Arecibo Radio Observatory as part of the First Light Team for the 12 meter VLBI reference antenna and the National Radio Astronomy Observatory conducting research on high speed serial analog to digital conversion architectures and the effect of alloy purity on conductivity at cryogenic temperatures. He has also collaborated with scientists and engineers from the University of New Mexico, the Naval Research Laboratory, NASA's Goldstone Deepspace Communications Complex, The Greenbank Radio Observatory, and NASA's Jet Propulsion Laboratory in his design research for the CARA's Low Frequency All Sky Monitor(LoFASM) radio telescope as well as with SpaceX engineers as part of STARGATE's first Student Group, SG-1.

James' areas of expertise include RF and microwave receivers, analog electronics, EM radiation and propagation, problem solving, and innovation. Although he loves collaborative research, and tackling difficult problems, what he enjoys the most spending time with his beautiful wife Sarah and son James II at his home located at 2354 Old Spanish Trail in Brownsville, Texas 78520.